

Hydroelastic response of floating elastic discs to regular waves. Part 1. Wave basin experiments

F. Montiel^{1,†}, F. Bonnefoy², P. Ferrant², L. G. Bennetts³, V. A. Squire¹
and P. Marsault⁴

¹Department of Mathematics and Statistics, University of Otago, P.O. Box 56,
Dunedin 9054, New Zealand

²Laboratoire de recherche en Hydrodynamique, Énergétique et Environnement Atmosphérique,
École Centrale de Nantes, 1 rue de la Noë, Nantes, France

³School of Mathematical Sciences, University of Adelaide, Adelaide, South Australia 5005, Australia

⁴Lycée François-Philibert Dessaignes, 12 rue Dessaignes, 41000 Blois, France

(Received 9 October 2012; revised 20 January 2013; accepted 24 February 2013;
first published online 16 April 2013)

A series of wave basin experiments is reported that investigates the flexural response of one or two floating thin elastic discs to monochromatic waves. The work is motivated by numerical model validation. Innovative techniques are used to ensure the experimental configuration is consistent with the model. This demands linear motions, time-harmonic conditions, homogeneity of the plate and the restriction of horizontal motions of the disc or discs. An optical remote sensing device is employed to record the deflection of the discs accurately. Tests involving a single disc and two discs are conducted for a range of disc thicknesses, incident wave steepnesses, frequencies and, in the case of two discs, geometrical arrangements. A data processing technique is used to decompose the raw data into its spectral harmonics and filter the higher-order components. Pointwise comparisons of the linear first-order component of the experimental deflection with numerical predictions are presented. Satisfying agreement is found, although the model consistently over predicts the deflection. Disc–disc interactions are observed in the two-disc tests. A brief discussion of the shortcomings of the pointwise analysis, with associated possible sources of discrepancy, provides a link to the study reported in Part 2 (Montiel *et al. J. Fluid Mech.*, vol. 723, 2013, pp. 629–652).

Key words: wave scattering, wave–structure interactions, waves/free-surface flows

1. Introduction

The response of floating *rigid* structures to ocean surface waves has received considerable attention for over 100 years, driven primarily by the expanding needs of the world's navies and their allied industries (Wehausen 1971). Notwithstanding these advances, no floating structures are actually perfectly rigid and many flex appreciably due to the passing waves. Acknowledging that such deformations can sometimes be inelastic, the term hydroelasticity is used to describe such phenomena.

[†] Email address for correspondence: fmontiel@maths.otago.ac.nz

Flexural motion becomes important in situations where the hydrodynamic loads impose significant strains on the structure, e.g. for sloshing impacts and vibrational properties of ships (Bishop & Price 1979; Faltinsen & Timokha 2009; Hirdaris & Temarel 2009; Wu & Cui 2009; Ten, Malenica & Korobkin 2011), and for the fracture of sea-ice in the polar regions. A particular consequence of flexural motion is that waves may propagate through the hydroelastic system as oscillations in the fluid–structure interface. Yet, despite its importance, the topic of hydroelasticity has been comparatively less well studied, especially experimentally.

It is appropriate, therefore, that the research reported herein focuses on the response of compliant floating structures to linear waves. The structures are characterized by thicknesses significantly smaller than their horizontal dimensions. Thin elastic structures are the basis of two contemporary research areas: first, the design of compliant pontoons or mat-like very large floating structures (VLFSs); and, second, for modelling interactions between ocean waves and sea-ice.

The latter application relates to the propagation of waves through the outer band of the ice-covered polar ocean, known as the marginal ice zone (MIZ), which is a vast collection of floes of diameters approximately equivalent to the dominant wavelengths (see the recent reviews of Squire 2007, 2011). The elastic response of the floes to wave forcing is a fundamental modelling consideration, as it creates so-called flexural-gravity waves that are believed to be the dominant cause of floe breaking (Langhorne *et al.* 1998; Toyota, Haas & Tamura 2011).

The Mega-Float test model for a floating runway in Tokyo Bay (Suzuki 2005), and other related projects, have provided motivation for hydroelastic analysis of VLFSs (see the review of Watanabe, Utsunomiya & Wang 2004). Research is undertaken, e.g. for the development of efficient mitigating techniques to minimize the structure's motion (Wang *et al.* 2010).

There are clear modelling parallels between wave interactions with VLFSs and sea-ice (Squire 2008). Both research areas recognize the critical lack of experimental data to support the expanding corpus of theoretical research (Chen *et al.* 2006; Squire 2007).

A unique set of wave basin experiments are reported in the current paper. The experiments characterize the flexural motion of one and two floating thin elastic discs. We describe a new experimental procedure to record the deflection over the surface of the discs remotely for a range of wave frequencies, wave steepnesses and disc thicknesses. The experimental data are used to validate the standard hydroelastic model of thin discs under regular wave forcing. The experimental procedure is designed to reproduce the limitations of the numerical model as a means to conduct a proper validation analysis. To the best of the authors' knowledge, no past experimental campaigns have tested the suitability of the thin elastic plate model for the three-dimensional configuration considered here.

The standard model referred to above uses a combination of thin elastic plate theory for the discs (Love 1944) and a potential flow for an incompressible and inviscid fluid domain. Under time-harmonic conditions, a monochromatic incident wave train sets the disc or discs in motion. The waves are of small amplitude compared with the wavelength and linearity is applied to the motion of the fluid and the discs. The discs are allowed to move freely in the vertical direction but in-plane rigid-body motions (surge, sway and yaw) are neglected. These restrictions and simplifying assumptions are important as they delineate the requisite experimental set-up. In addition, semi-analytical solutions can be found under these conditions (see Meylan & Squire 1996; Peter, Meylan & Chung 2003; Andrianov & Hermans 2005, for the

single disc problem). Our analysis extends these previous works, as we account for Archimedean draught of the disc.

Experimental programmes were also conducted in Japan in the late 1990s to characterize the hydroelastic response of rectangular elastic structures under regular wave forcing, intended to replicate VLFSs at the basin scale. Typically, composite compliant structures were used to simulate the flexural motion of the VLFSs being modelled (Ohmatsu 2008). The composites are not vertically uniform (violating the thin-plate assumption), and are made of a heavy material with significant rigidity (e.g. aluminium plate), which is fixed on top of a buoyant material (e.g. polyethylene), assumed to have negligible mass and rigidity. Under these conditions, tests have been conducted to measure the elastic motion in the structure and compare the results with numerical predictions (see, e.g., Utsunomiya *et al.* 1995; Yago & Endo 1996; Kagemoto, Fujino & Murai 1998).

In relation to wave/sea-ice interaction research, very few experimental investigations have been conducted to characterize the scattering by thin elastic structures in a laboratory setting. Squire (1984) and Meylan (1994) attempted two-dimensional experiments in a wave flume but failed to obtain reliable data due to perturbations induced by the reflected waves from the beach and flooding events. The only series of tests that is relevant to the present work were conducted by Sakai & Hanai (2002) in a 26 m-long wave flume. The investigators used elastic sheets made of polyethylene (with thicknesses 5 and 20 mm) as a substitute for ice, thereby allowing for bending motion. They were able to measure the deflection of several arrangements of adjacent plates at a few regularly spaced points using ultrasonic sensors. They then determined an empirical dispersion relation for flexural-gravity waves travelling through quasi-continuous ice-covered seas. Later, Kohout *et al.* (2007) utilized the experimental data of Sakai & Hanai to validate the response of one, two and four floating beams, predicted by the two-dimensional version of the numerical model used in our investigation.

The kernel of our investigation concerns the response of a single disc. In this case, the experimental set-up consists of a compliant circular disc floating at the surface of a wave basin. The disc is equipped with appropriate additional components to comply with the restrictions imposed by the numerical model. The deflection of the disc is recorded using a remote sensing motion tracking device, providing time series of the vertical displacement at many points of the disc's surface. The influence of the transient regime, the basin boundaries and possible nonlinear effects is removed from the associated time series by a sliding-window Fourier analysis. We then obtain the linear steady-state amplitude of the deflection at each measuring point, which can be compared with the value predicted by the linear time-harmonic model. Extensions of the set-up and data analysis for two discs follow straightforwardly from those of the single disc.

A thorough description of the single-disc set-up is given in §2, including the measurement techniques and the novel technical solutions designed to impose appropriate restrictions on the disc's motion. An outline of the two-disc set-up and a discussion of the parameters varied as part of the campaign are also proposed. In §3, a preliminary comparative analysis involving unprocessed deflection data is proposed. It provides qualitative insights with regards to the form of the signals measured in comparison with the model predictions. In §4, a data processing technique, based on a sliding-window Fourier analysis, is derived for the measured time series. The method is used to check the repeatability of the experimental procedure. A selection of pointwise comparative results of the vertical displacement is presented

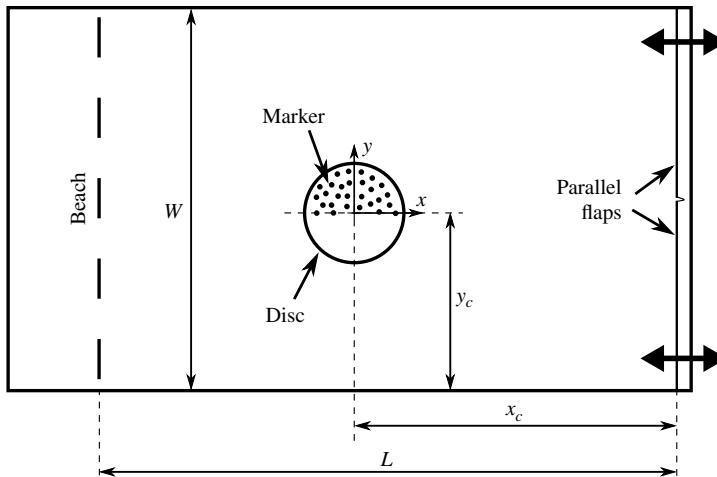


FIGURE 1. Simplified schematic of the wave basin and the single-disc set-up.

in § 5. We analyse the displacement at four different points for the single-disc case and investigate the proportion of second-order harmonic components on the motion. Results for the two-disc case are also given. Finally, a justification of the limitations of the pointwise comparative study conducted in this paper is given in § 6, which demonstrates the need for additional comparative analyses in terms of integrated quantities over the disc surface. This provides a link to the investigation presented in the companion paper to the current study (Montiel *et al.* 2013), hereinafter referred to as Part 2.

The work presented here and in Part 2 is a subset of that reported by Montiel (2012). Additional details regarding the design of the single-disc set-up are provided by Marsault (2010).

2. Experimental campaign

We conducted a series of experiments at the Laboratoire de recherche en Hydrodynamique, Énergétique et Environnement Atmosphérique of École Centrale de Nantes in a wave basin of length $L \approx 15.5$ m, width $W \approx 9.5$ m and depth $h \approx 1.9$ m. The wave basin is bounded in length by a wavemaker at one end and a beach at the opposite end. The wavemaker is unidirectional and is composed of two identical parallel hinged flaps controlled by a computer. In addition, the basin is equipped with two platforms attached to bridges moving on rails, allowing us to fix parts of the experimental set-up in the laboratory's frame of reference. A simplified schematic of the basin is given in figure 1.

2.1. Single-disc set-up

We set the origin of a Cartesian coordinate system $Oxyz$ to coincide with the centre of the disc and the free surface at rest. The z -axis points vertically upwards. The x -axis is parallel to the sidewalls and points towards the wavemaker. We use x_c and y_c to denote the distance from the disc centre to the wavemaker and the closest sidewall, respectively (see figure 1).

A material with suitable density and elastic properties must be chosen to test the validity of the thin elastic plate model experimentally. We used an expanded polyvinyl

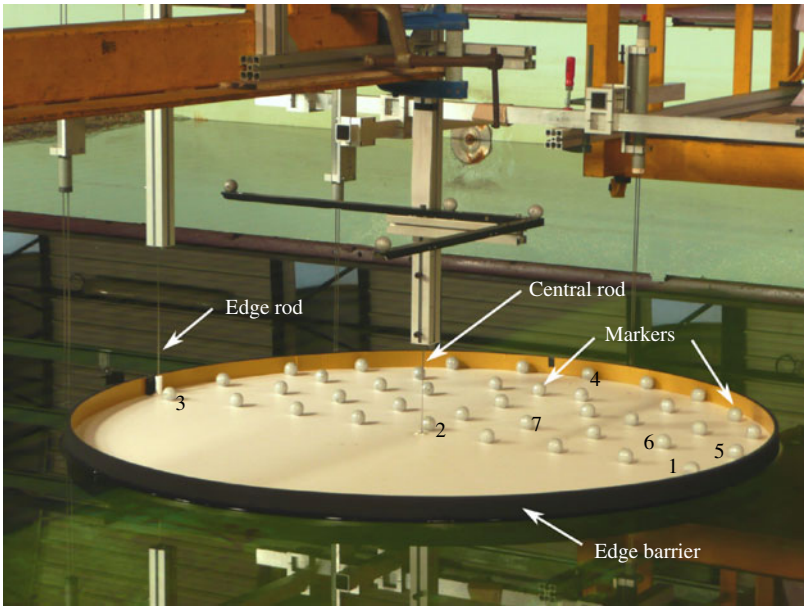


FIGURE 2. (Colour online) Snapshot of the experimental set-up for a disc of thickness $D = 10$ mm. Seven markers are labelled for reference throughout the paper.

D (mm)	E_{exp} (MPa)	E_{spec} (MPa)	ρ_{exp} (kg m ⁻³)	ρ_{spec} (kg m ⁻³)	ν
3	838	1300	623	700	0.3
5	503	750	547	500	0.3
10	496	750	530	500	0.3

TABLE 1. Properties of the expanded PVC.

chloride (PVC) FOREX[®], which is known to be reasonably compliant. Discs of radius $R = 0.72$ m were formed by a high-precision milling procedure from PVC sheets of thickness $D = 3, 5$ and 10 mm. We determined experimentally the density, ρ , and Young’s modulus, E , of the PVC to compare with the values specified by the manufacturer. A series of four-point bending tests was conducted to measure the Young’s modulus (see Marsault 2010). A summary of the properties of the PVC relevant to the present study is given in table 1, where the subscripts ‘*exp*’ and ‘*spec*’ denote values of the parameter measured experimentally and specified by the manufacturer, respectively. It is assumed here that the Young’s modulus does not depend on frequency. The influence of this parameter will be considered in Part 2. Poisson’s ratio, ν , is also indicated and is set to a typical value for polymeric foams of 0.3, which coincidentally is also commonly taken for sea-ice and VLFS models. Figure 2 shows the 10 mm disc and part of the experimental equipment that we discuss subsequently.

A significant feature of the experimental set-up consists of enforcing the restriction of the surge, sway and yaw components of the motion of the disc, consistent with the

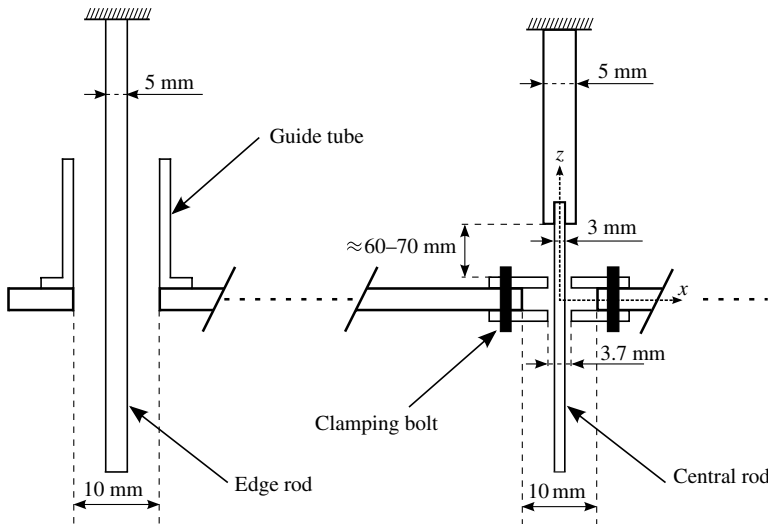


FIGURE 3. Cross-sectional view of the mechanical device used to restrict the disc's motion in the xy -plane (not to scale).

numerical model's simplifying assumptions. In addition, these restrictions are required to allow accurate measurements of the disc deflection to be made (see § 2.2). A mechanical device was designed to comply with these requirements. It is composed of two vertical aluminium rods. The rods are fixed from their upper end to the platform. One rod, of diameter 3 mm, goes through a hole in the disc at its centre to inhibit horizontal oscillations, and is referred to as the central rod. The second rod, referred to as the edge rod, has a diameter of 5 mm and goes through the disc on the x -axis close to the edge ($x < 0$, $y = 0$). Mitigation of yaw motion is then achieved by the coupled action of the rods. The rods are indicated in figure 2. Both rods have their lower end free and located approximately 0.15 m under the disc's lower surface.

Figure 3 shows a schematic of the cross-sectional view of the two-rod arrangement. The edge rod is guided through a hole in the disc by a thin tube. We found that setting a 2.5 mm clearance is sufficient to mitigate the yaw rotation and to reduce the contact between the rod and the tube, which is a potential source of friction in the motion. On the other hand, we minimize the horizontal oscillations by setting a 0.35 mm clearance around the central rod. The guide is composed of two vertically aligned aluminium plates, fixed on each side of the disc, which are pierced by a 3.7 mm diameter hole. Note that the disc itself has a much larger hole (10 mm), which reduces the surface of contact between the rod and its guide. The reduced clearance allows for better guidance than for the edge rod, but increases frictional effects arising from the contact between the rod and its guide when the system is set in motion. To reduce friction due to the rod bending under surge- and sway-induced forces, we minimize the distance between the clamped upper end of the rod and the disc, allowing for sufficient vertical clearance to avoid contact during tests with relatively high-amplitude waves. Although significant efforts have been put into moderating frictional effects, their influence on the motion is unclear and will be discussed further (see Part 2).

Preliminary basin tests showed that flooding events occur under wave forcing, which induce additional loads acting on the top surface of the disc, and that are usually referred to as green water loads. These loads are not included in our hydroelastic

model as they originate from highly nonlinear phenomena. To prevent such loads from affecting the response of the disc, we installed a barrier around the edge of the disc. We used adhesive strips (with rectangular cross-section) of neoprene foam (waterproof synthetic rubber), fixed around the circular contour of the disc. For the 5 and 10 mm discs, the strip is stuck over the circular side surface, providing a barrier of height 50 mm. On the other hand, the 3 mm disc did not provide a side surface sufficiently large to stick the strip. In this case, the strip rests on the top surface of the disc along the contour.

The edge barrier is shown in figure 2 for the 10 mm disc. The influence of the barrier on the response of the disc (in terms of adding an extra weight and stiffening the structure along the edge) is difficult to estimate experimentally, but a theoretical investigation of its effect is presented in Part 2.

2.2. Measurements

The amplitude of the waves generated by the wavemaker is recorded using resistive wave gauges. Five gauges are located in the vicinity of the disc position in the basin, and the incident wave data are collected during tests with no discs. This allows us to feed the numerical model accurate incident wave amplitudes required for comparisons with experimental data. Note that the wave measurements are accurate to $O(10^{-4} \text{ m})$.

The goal of the present experiment is to measure the deformation experienced by the disc under wave forcing. The deflection is recorded by a motion tracking device composed of three infrared (IR) cameras that capture the three-dimensional position of markers over time by stereoscopy. The markers are polystyrene spheres of diameter 30 mm, covered with a retro-reflective tape (detectable by the IR cameras), which are fixed to the surface of the disc, as shown in figure 2. The motion tracking device is developed by Qualisys® and includes the software package Qualisys Track Manager (QTM 2009, v2.3, Qualisys AB, Sweden) for the reconstruction of the stereoscopic data as well as the control of the calibration and acquisition procedures.

Assuming symmetry with respect to the x -axis, deflection measurements are only required on half the disc. An optimal grid of 39 markers covering half the disc was found (Marsault 2010), such that all of the markers are seen at all times by the three IR cameras utilized during the tests. In results not shown here, we have shown that the relative difference in displacement between two symmetric markers is less than 3 % in most cases, thereby validating the symmetry assumption. Note that the restriction of yaw motion is necessary to force the markers to remain in the same half-plane during the tests. Minimizing horizontal oscillations also improves the accuracy of the measured data. Analyses of experimental data have shown that the amplitude of these motions is limited to one order of magnitude less than that of the incident wave amplitude.

Each marker weighs approximately 3 g so that the markers-to-disc weight ratios are 3.5 %, 2.6 % and 1.4 % for the 3, 5 and 10 mm discs, respectively. The hydrostatic equilibrium is then slightly modified as the draught is increased. The influence of the extra draught on the motion of the disc is, however, insignificant (Montiel 2012). Therefore, the effect of the markers is neglected throughout this study.

The camera set-up is shown in figure 4. Two cameras are located along a sidewall of the wave basin (see figure 4a) and the third camera is fixed to a bridge above the disc and points downwards (see figure 4b). The initial position of the markers is found after calibration of the motion tracking device. This procedure consists of determining the accurate location of four reference markers fixed onto an L-shaped frame (see figure 4a), set approximately 0.4 m above the disc, which constitutes the

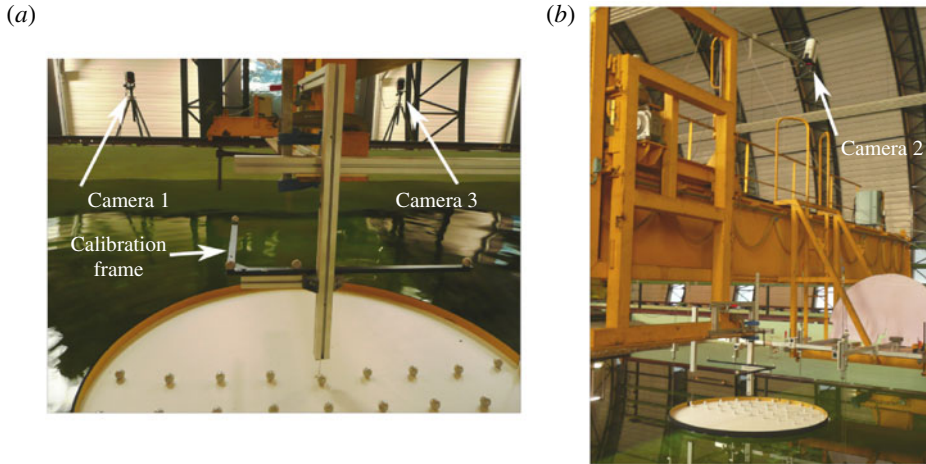


FIGURE 4. (Colour online) Two snapshots of the experimental set-up displaying (a) the two IR cameras positioned on the side of the wave basin and the calibration frame and (b) the third camera located above the disc.

frame of reference of the device. Note that this measuring device provides accurate data to $O(10^{-5}\text{--}10^{-4}\text{ m})$.

The stereoscopic measurements of the disc's motion are directly controlled by the QTM software. A sampling frequency of 64 Hz is used for the acquisition procedure, which is launched by an external trigger, this being the wavemaker control software. QTM generates data files (.mat) to be analysed by MATLAB, containing the coordinates of each marker at each time step in the reference frame defined by the calibration frame. Knowing the location of the markers with respect to the disc centre then allows us to express the coordinates of the markers in the system $Oxyz$ defined previously.

2.3. Two-disc set-up

Consider the case of two discs with spacing s (centre to centre) and angle ϖ (with respect to the x -axis), as shown in figure 5. The objective is to measure the deflection of the two discs in their four halves (regions 1–4). As the incoming wave is propagating from right to left in figure 5, we refer to the rightmost disc as the front disc and the leftmost one as the back disc.

The IR cameras used to capture the location of the markers have a limited field of view and optical resolution (ability to distinguish two markers close to each other), so that we cannot use a single arrangement of cameras to locate markers on two different discs accurately. This requires each test to be performed twice (one disc analysed at a time).

For symmetric arrangements (i.e. $\varpi = 0$), the deflection in regions 2 and 4 need not be measured, so that only two tests are required. For non-symmetric arrangements (i.e. $0 < \varpi < \pi/2$), the motion in regions 2 and 4 must be measured independently from that in regions 1 and 3. Preliminary tests showed that markers located close to the edge barrier in regions 2 and 4 could not be seen by the two cameras on the side of the basin. Therefore, the motion in region 2/4 is obtained by translating the up-wave/down-wave disc into the lower/upper half plane, preserving spacing and angle.

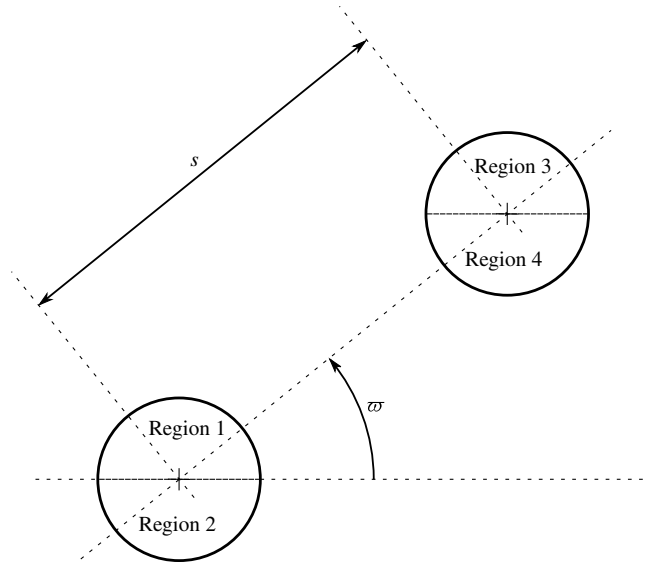


FIGURE 5. Experimental arrangement involving two discs. Four regions representing half a disc are defined.

The influence of the sidewalls may be critical in this experiment, as for certain angles a disc may be close to a wall and interact with it in a way that affects its response. Particular care must be taken while analysing the data to detect and ameliorate such effects.

2.4. Summary of tests achieved

We operate the wavemaker to generate regular waves in the frequency range $f_0 = 0.6\text{--}1.3$ Hz, with corresponding wavelengths in the range $\lambda \approx 0.9\text{--}4.3$ m. The amplitude A of each wave generated is determined by the steepness, defined here as $\varepsilon = 2A/\lambda$. Tests are conducted for approximate steepnesses 1 and 2 %, allowing us to check the validity of the linearity assumption. For the ratios of the wavelengths to the disc diameter considered here, the discs may be regarded as large and diffraction effects are significant. Specifically, the non-dimensional wavenumber takes values in the range $ka \approx 1\text{--}5$, where $k = 2\pi/\lambda$ and $a = R$. We conducted tests for a range of eight frequencies (see table 2). The values of kh displayed in table 2 show that deep-water wave conditions ($kh \gg 1$) apply over most of the frequency range.

Tests were conducted for eight frequencies. The parameter values for the incident wave are given in table 2. The amplitudes given here are provided by the incident wave measurements (tests with no discs), conducted with the group of five wave gauges at two locations $x \approx 7$ m and $x \approx 10.5$ m.

Two series of experiments were carried out that involve a single disc, corresponding to two positions of the disc in the wave basin, $x_c \approx 7$ m and $x_c \approx 10.5$ m. This allows us to check the potential variability of the disc response with the distance from the wavemaker due to that of the generated wave field (e.g. higher-order harmonics and noise). The repeatability of the experimental procedure can then be deduced. At each location, we conducted tests for three disc thicknesses, $D = 3, 5$ and 10 mm, two wave steepnesses and eight frequencies, as mentioned above. For the single-disc experimental campaign 96 tests were performed.

f_0 (Hz)	0.6	0.7	0.8	0.9	1	1.1	1.2	1.3
λ (m)	4.3	3.2	2.4	1.9	1.6	1.3	1.1	0.9
ka	1.0	1.4	1.9	2.4	2.8	3.5	4.1	5.0
kh	2.7	3.7	4.9	6.2	7.4	9.1	10.7	13.1
A_1 % (mm)	22.3	15.6	12.6	9.9	8.2	6.8	5.4	4.5
A_2 % (mm)	44	30.8	25.1	20.1	16.6	13.8	10.8	8.8

TABLE 2. Wave conditions for the single-disc series of tests.

Tests involving two discs were performed on a limited range of parameters, due to the two additional parameters involved (s and ϖ). Consequently, we only considered two disc thicknesses, $D = 3$ and 10 mm, and one wave steepness, $\varepsilon \approx 1\%$. However, we conducted the analysis on the whole range of eight frequencies, as for the single disc experiment. Four two-disc arrangements have been tested that allow us to test the influence of the spacing on a symmetric configuration and the angle for a given spacing. Two symmetric arrangements with respect to the x -axis (i.e. $\varpi = 0$) were tested with $s = 1.88$ m and $s = 3$ m. For non-symmetric arrangements, we set the spacing $s = 3$ m and performed tests for $\varpi = 30^\circ$ and $\varpi = 45^\circ$. A total of 64 experimental tests were conducted with two discs, using incident wave data determined for the single disc experiment, recalling that two and four tests are required for each symmetric and non-symmetric arrangements, respectively.

3. Preliminary comparisons

In this section, we are concerned with the response of a single disc. Results for a two-disc system will be given § 5.3.

3.1. Numerical model

Under the simplifying assumptions outlined in § 1, we derive a model for the time-harmonic response of a floating thin elastic disc. The model is identical to that used by Peter *et al.* (2003), with the addition that the draught of the plate, d say, is included. From Archimedes' principle, $d = (\rho/\rho_0)D$, where $\rho_0 \approx 1000$ kg m⁻³ is the density of the fluid. The motion of the fluid is described in terms of the velocity potential $\Phi(\mathbf{x}, t) = \text{Re}\{\phi(\mathbf{x})e^{i\omega t}\}$, where ω is the radian frequency and the (reduced) potential ϕ is complex-valued. Cylindrical coordinates, $\mathbf{x} = (r, \theta, z)$, are used to denote the location of points in the fluid domain. The horizontal coordinates, (r, θ) , are related to the Cartesian coordinates (x, y) defined earlier via $x = r \cos \theta$ and $y = r \sin \theta$.

The potential, ϕ , satisfies Laplace's equation throughout the fluid domain, Ω , and a no-flow condition over the seabed surface, i.e.

$$\Delta\phi = 0 \quad (\mathbf{x} \in \Omega) \quad \text{and} \quad \partial_z\phi = 0 \quad (z = -h). \quad (3.1a)$$

Additional conditions hold on the upper surface of the fluid domain. The motion of the free surface is governed by

$$\partial_z\phi = \alpha\phi \quad (r > R, z = 0), \quad (3.1b)$$

where $\alpha = \omega^2/g$ and $g \approx 9.81$ m s⁻² is acceleration due to gravity. At the disc/fluid interface, the potential satisfies

$$(\beta\nabla^4 + 1 - \alpha d) \partial_z\phi = -\alpha\phi \quad (r \leq R, z = -d), \quad (3.1c)$$

where $\beta = F/\rho_0 g$, with $F = ED^3/12(1 - \nu^2)$ the flexural rigidity. The vertical displacement w of the disc is obtained through the kinematic condition on the plate's underside, $w(r, \theta) = (1/i\omega)\partial_z\phi(r, \theta, -d)$. Free-edge conditions, representing the vanishing of bending moment and shearing stress, are also applied. They are expressed as

$$\left[r^2\nabla^2 - (1 - \nu)(r\partial_r + \partial_\theta^2)\right]\partial_z\phi = \left[r^3\partial_r\nabla^2 + (1 - \nu)(r\partial_r - 1)\partial_\theta^2\right]\partial_z\phi = 0, \quad (3.1d)$$

respectively, for $r = R$ and $z = -d$. The inclusion of draught adds the final condition

$$\partial_r\phi = 0 \quad (r = R, \quad -d < z < 0), \quad (3.1e)$$

which imposes no flow through the submerged portion of the disc.

We derive eigenfunction expansions for the solution using separation of variables in the free-surface and plate-covered fluid regions. Specifically, the displacement of the disc/fluid interface is given by

$$w(r, \theta) = \sum_{p=-2}^{\infty} \sum_{n=-\infty}^{\infty} B_{p,n} I_n(\kappa_p r) e^{in\theta} \quad (r \leq R). \quad (3.2)$$

Here I_n denotes the modified Bessel function of the first kind of order n and $B_{p,n}$ denote unknown amplitudes that are determined by the solution method, which is outlined in Part 2. The wavenumbers κ_p , $p \geq -2$, are roots of the dispersion relation

$$(\beta\kappa^4 + 1 - \alpha d) \kappa \tan \kappa(h - d) = -\alpha. \quad (3.3)$$

We obtain numerical values for the displacement at any point of the plate from (3.2), by truncating the infinite sums, so that the required level of convergence is achieved. The theoretical results presented in this paper are given with an accuracy of at least two decimal places (for a unit incident wave amplitude), which is more than satisfactory given the accuracy of the experimental measurements.

3.2. Model/data comparisons

The time-harmonic response of the system is equivalent to its oscillatory steady state under a transient regular wave forcing from rest, which characterizes the wavemaker forcing in our tests. We designate steady-state conditions in the wave basin by defining a time window that starts after the initial wavefront has passed, t_1 say, which can be estimated roughly as x_c/G_g , where C_g is the group velocity of the wave generated.

Although the beach acts as a dissipation zone, it reflects a non-negligible proportion of the incoming waves (reflection coefficient of 5–15 % depending on the frequency; see Marsault 2010). However, waves reflected by the sidewalls will interfere with the motion of the disc prior to that of the beach. To avoid contamination of the data by the reflected waves, we truncate the time series at a maximum time, t_2 say, corresponding to the estimated time at which reflected waves from the closest boundary (here the closest sidewall) disturb the disc motion. Theoretical estimates are given by $t_2 = (x_c + 2y_c)/C_g$.

Table 3 shows the values of t_1 and t_2 for each frequency and both disc locations. The time window bounded by t_1 and t_2 corresponds to a rough estimate of the steady-state regime in an unbounded fluid domain. For each test conducted, we define a proper steady-state window $(t_1 + \delta_1 T_0, t_2 - \delta_2 T_0)$, where T_0 is the incident wave period and the non-dimensional coefficients δ_1 and δ_2 are adjusted manually to capture the constant portion of the signal in the interval (t_1, t_2) .

f_0 (Hz)	0.6	0.7	0.8	0.9	1	1.1	1.2	1.3
C_g (m s ⁻¹)	1.34	1.12	0.98	0.87	0.78	0.71	0.65	0.60
$x_c \approx 10.5$ m								
t_1 (s)	7.9	9.5	10.9	12.2	13.6	15	16.4	17.7
t_2 (s)	14.2	17	19.4	21.9	24.4	26.9	29.3	31.6
$x_c \approx 7$ m								
t_1 (s)	5.3	6.3	7.2	8.1	9.1	10	10.9	11.7
t_2 (s)	11.8	14.1	16.1	18.2	20.3	22.3	24.4	26.3

TABLE 3. Theoretical estimate of the start and end times of the steady-state window for each frequency and each disc location.

3.2.1. Pointwise comparisons

We perform initial comparisons for the deflection of marker 2 (see figure 2) between the raw time series provided by the motion tracking device, denoted by $z_2(t)$, and the model's predictions. To ensure that the compared signals are in phase, the theoretical and experimental deflections have to be synchronized by means of the phase of the incident wave. Under steady wave generation, the time delay of the experimental incident wave in reaching the centre of the disc is given by

$$t_\varphi = t_d - x_c/C_\varphi, \quad (3.4)$$

where $t_d = 0.93$ s is the wavemaker trigger delay (inherent to the device) and $C_\varphi = \omega/k$ is the phase velocity of the incident wave. Therefore, the appropriate synchronization is obtained by multiplying the theoretical deflection by $\exp(i\omega t_\varphi)$, so that the time-harmonic deflected surface is given over time as

$$W(r, \theta, t) = \text{Re} \left\{ w(r, \theta) e^{i\omega(t+t_\varphi)} \right\}. \quad (3.5)$$

Figure 6 shows a comparison of the theoretical and experimental time series of $z_2(t)$ over a time interval that contains the steady-state window. The signals are compared for the three thicknesses $D = 3, 5$ and 10 mm, at four different frequencies $f_0 = 0.6, 0.8, 1.1$ and 1.3 Hz, for a steepness $\varepsilon \approx 1\%$ and the disc location $x_c \approx 7$ m. The time-harmonic signals predicted by the numerical model are obtained for incident wave amplitudes provided by table 2. We observe that once the experimental signal has reached its steady state, it is in phase with the theoretical harmonic signal. This also suggests that the dispersion properties of the disc-covered region in experiments and model agree. However, tests on larger disc-covered regions would be required to make a conclusive statement on the dispersion properties.

In terms of amplitude, we observe a reasonable agreement in the steady-state window for all cases considered, suggesting that the experimental set-up described in §2 provides sensible data. In particular, the experimental (at steady state) and theoretical time series coincide for the 3 mm disc. For the 5 and 10 mm discs, the numerical model slightly overestimates the amplitude measured experimentally. On the other hand, the amplitudes of the experimental signals become more variable over time as the frequency increases (and therefore as the magnitude of the motion decreases),

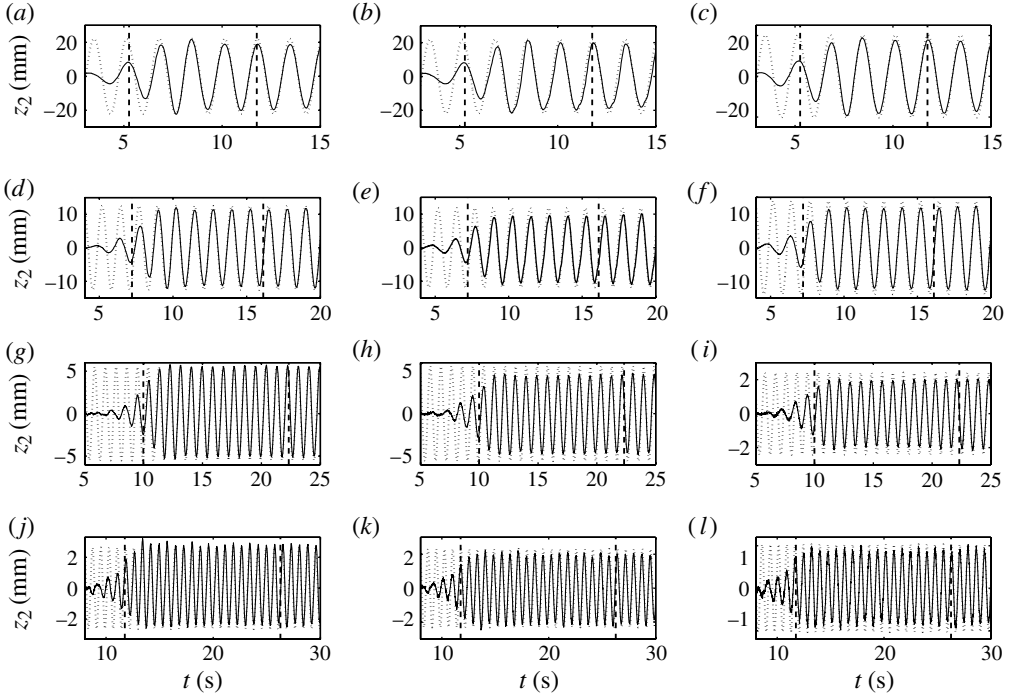


FIGURE 6. Time-dependent deflection of marker 2 for (a–c) $f_0 = 0.6$ Hz, (d–f) $f_0 = 0.8$ Hz, (g–i) $f_0 = 1.1$ Hz and (j–l) $f_0 = 1.3$ Hz. For each frequency considered, the time series are plotted for (a,d,g,j) $D = 3$ mm, (b,e,h,k) $D = 5$ mm and (c,f,i,l) $D = 10$ mm. The dataset obtained for the wave steepness $\varepsilon \approx 1\%$ and the disc location $x_c \approx 7$ m are used. In each figure, the corresponding theoretical time-harmonic signal is given (dotted line) for comparison and the characteristic times t_1 and t_2 are shown as vertical dashed lines.

suggesting that nonlinearities, such as noise or higher-order harmonics, affect the response of the disc.

3.2.2. Visual comparisons

We extend the pointwise comparisons to analyse the response of the full disc. This provides a step towards our ultimate goal of characterizing the flexural motion of the disc, as discussed in §1. Using the deflection data of all of the markers and their symmetric images, we can interpolate the displacement at any point of the disc. This allows us to obtain the deflection of the whole disc from the data of 39 points only. A visual comparison of disc deflections then provides qualitative insights on the agreement regarding the bending motion of the disc. We form a regular polar grid composed of 2921 nodal points, at which we estimate the deflection by bilinear interpolation.

Figure 7 shows the deflection surfaces $W(r, \theta, t)$ obtained experimentally and theoretically for the 5 mm-thick disc at $f_0 = 0.8$ Hz and $f_0 = 1.1$ Hz, for $\varepsilon \approx 1\%$ and $x_c \approx 7$ m. The experimental surfaces are shown at $t = 14.7$ s and $t = 18.2$ s for $f_0 = 0.8$ Hz and $f_0 = 1.1$ Hz, respectively, i.e. within the steady-state window. We find a good agreement in terms of phases for both cases, extending the observations from the pointwise comparison shown in figure 6 to the disc surface.

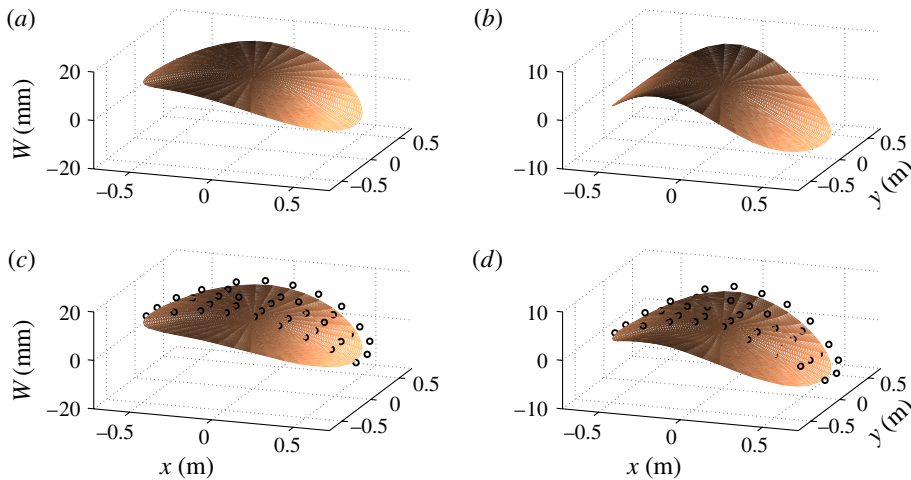


FIGURE 7. (Colour online) Deflection of the 5 mm disc for a wave steepness $\varepsilon \approx 1\%$, $x_c \approx 7$ m and frequencies (a,c) $f_0 = 0.8$ Hz and (b,d) $f_0 = 1.1$ Hz. For each frequency, the theoretical time-harmonic deflection (a,b) is compared with the deflection obtained by interpolation from the experimental data (c,d). The deflection surfaces obtained experimentally are shown at $t = 14.7$ s and $t = 18.2$ s for $f_0 = 0.8$ Hz and $f_0 = 1.1$ Hz, respectively. The circles on the experimental surfaces represent the markers.

It is more difficult to quantify the agreement between the experimental and theoretical deflection surfaces in terms of amplitudes. We observe that the numerical model slightly overestimates the response for both frequencies, generalizing the results found for marker 2 to the whole disc surface. In addition, the theoretical surfaces display a higher degree of curvature than those obtained from the experimental data, especially near the disc edge on the y -axis.

The good qualitative agreement between the theoretical and experimental deflected surfaces provides evidence that the experimental set-up performs reasonably well. Additional analyses are required to interpret the agreement over the frequency range considered and filter potential nonlinear components contained in the measured time series. The data processing technique devised in §4 generates data that are consistent with the linearity assumption of the model.

4. Data analysis

4.1. Fourier analysis

Although we conducted tests at low incident wave steepness ($\varepsilon \ll 1$), nonlinearities may arise from unexpected sources, due to imperfections of the set-up or the wavemaker. In particular, the time series obtained for each marker and the wave gauge may be contaminated by higher-order harmonics and noise due to external perturbations or inherent to the measuring devices. Therefore, we seek to filter wave components of frequency higher than the frequency of excitation, and extract the linear first-order part of the time series to improve comparisons with theoretical predictions.

We decompose each time series into its frequency domain Fourier components using a discrete Fourier transform (DFT). Evaluating the DFT components within a time window provides the spectral decomposition of the signal at a given time. By repeating this procedure on successive windows over the duration of the test, we obtain the

time variations of each spectral component. This is a discrete version of the short-time Fourier transform (STFT) (see, e.g., Allen & Rabiner 1977; Cohen 1989). Given a time series, the STFT processing algorithm is outlined as follows:

- (i) Multiply the time series by a rectangular window sampled properly (equally spaced and including the end points) and centred at t with width T , which is taken to be an integer number of wave period.
- (ii) Compute the DFT components of the windowed time series using the fast Fourier transform (FFT). This is the discrete convolution of the signal's DFT with the window function's DFT.
- (iii) Select the first-order amplitude associated with the fundamental frequency, f_0 say, to extract the linear component.
- (iv) Discretize the time domain of the duration of the test and repeat the procedure described in (i)–(iii) successively at each time step.
- (v) Take the mean value over the steady-state window (defined in § 3.2), which represents the linear time-harmonic amplitude, free of the effects of the transient regime and the basin boundaries.

The efficiency of the STFT method is mainly determined by its resolution. The frequency resolution of the window function (ability to distinguish between two frequency components close to each other) is best for a rectangular window (Chu 2008), which motivates our choice for the window function. The time resolution is characterized by the duration of the window, T , as the associated spectral decomposition is well localized in time within a short window, i.e. sudden variations of the signal over time are captured. Reducing the window duration decreases the frequency resolution, however, which is known as the Gabor limit (a signal cannot be both time-limited and band-limited; see Cohen 1989). For the time series analysed here, we favour increasing the time resolution by taking a window duration of, typically, twice the period of the incident wave, i.e. $T = 2T_0$. This allows us to characterize the steady-state window accurately in time, which is critical to define a reliable time-harmonic experimental amplitude.

In order to illustrate numerically the spectral properties of a typical measured time series, and the STFT method, we consider the vertical displacement of the central marker (marker 2, see figure 2). The unprocessed vertical displacement is denoted by $z_2(t)$. We analyse the test defined by the following parameters: $\varepsilon \approx 1\%$, $f_0 = 0.8$ Hz, $D = 5$ mm and $x_c \approx 7$ m. Using steps (i)–(iv) of the STFT algorithm, the signal $Z_2^T(f, t)$ is calculated for frequencies f that are multiples of the sampling frequency $1/T$ ($1/T, 2/T, \dots$), where the higher-order components are obtained by extending step (iii) of the algorithm. As indicated above, the window duration is set to be twice the period of the wave generated. A time step of 0.2 s is used between successive windows.

In figure 8(a) the processed data are analysed in the form of a spectrogram, which is a three-dimensional display of the time-varying spectral decomposition of a signal. We set $f_{\max} = 10$ Hz as the upper boundary of the frequency domain and the grey colour map characterizes the amplitude $|Z_2^T(f, t)|$, such that the saturation is reached at its maximum for $f \in [0, 10]$ and $t \in [0, 25]$. The characteristic times t_1 and t_2 are also given as an estimate of the steady-state window (see § 3.2). As expected, we observe that, for $t > 9$ s (i.e. after the wavefront has passed), the signal's frequency content is dominated by the fundamental harmonic at f_0 (black strip). A second strip is also visible at $f = 2f_0 = 1.6$ Hz corresponding to the second-order harmonic, although

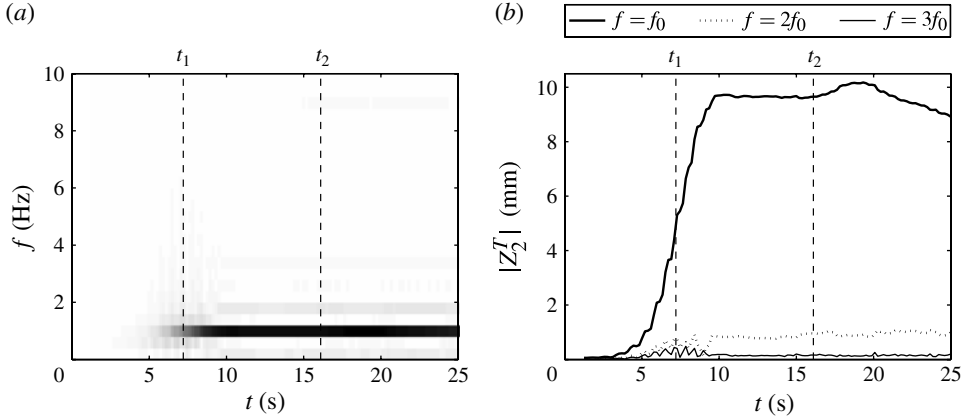


FIGURE 8. Short-time Fourier transform analysis of the vertical displacement of marker 5 for $\varepsilon \approx 1\%$, $f_0 = 0.8$ Hz, $D = 5$ mm and $x_c \approx 7$ m. The spectrogram of the signal and the cross-sectional views at $f = f_0$, $2f_0$ and $3f_0$ are shown in (a) and (b), respectively.

its magnitude is much lower (light grey) than that of the fundamental harmonic. To support the latter assertion, figure 8(b) shows the cross-sectional views of $|Z_2^T|$ at $f = f_0$ (thick solid line), $f = 2f_0$ (dotted line) and $f = 3f_0$ (thin solid line). It is clear again that the motion is dominated by the fundamental component during the steady-state window, defined by $t \approx 10$ – 15 s. This is confirmed quantitatively by the ratios $|Z_2^T(2f_0, t)/Z_2^T(f_0, t)| \approx 8\%$ and $|Z_2^T(3f_0, t)/Z_2^T(f_0, t)| \approx 1\%$ in the steady-state window. The influence of the second-order harmonic is not negligible, however, and will be analysed further in § 5.2.

Note that in further analyses, we define the steady-state window manually during step (v) of the STFT algorithm, based on the spectrogram reading corresponding to the time series analysed.

4.2. Repeatability of the measurements

We can estimate the inherent error of the wavemaker forcing, the measuring devices and the STFT method (reading error on the spectrogram due to the amplitude-averaging performed within the steady-state window) by analysing the variability of a measured quantity over a set of equivalent tests. The variability is quantified by the standard deviation of the corresponding measured values. For instance, we obtained 10 independent measurements of the incident wave amplitude (five wave gauge data at two locations) for each frequency and steepness, assuming that the presence of a gauge does not affect the wavefield measured by the adjacent gauges. The incident wave amplitudes, processed by STFT at each frequency, are given in table 2 for the steepnesses 1 and 2%. The standard deviation, calculated over the 10 values, provides an estimate of the error.

To determine the repeatability of the experimental procedure, we define the relative error of a data set $\mathcal{D} = \{(X_1, \dots, X_n), n \in \mathbb{N}, n \geq 2\}$, as the standard deviation to mean ratio, i.e.

$$\mathcal{E} = \frac{1}{\bar{X}} \sqrt{\frac{1}{n-1} \sum_{i=1}^n (X_i - \bar{X})^2}, \quad (4.1)$$

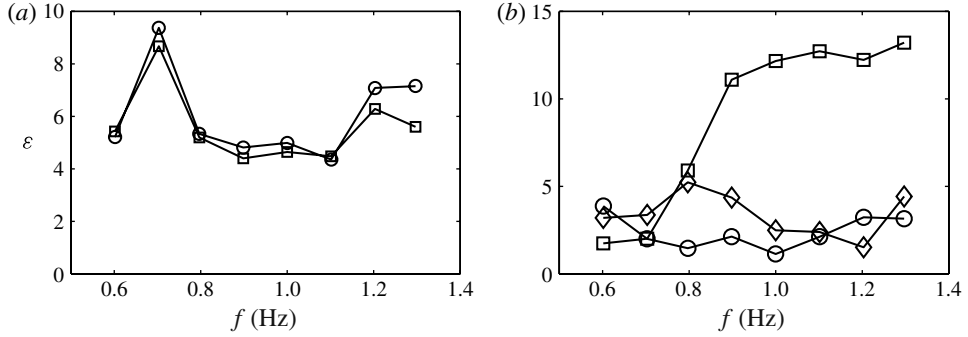


FIGURE 9. Relative error (percentage) of (a) the incident wave data and (b) the vertical displacement data of marker 2, as a function of frequency. In (a), the relative error is given for the wave steepnesses $\varepsilon \approx 1\%$ (circles) and $\varepsilon \approx 2\%$ (squares), and in (b), it is given for $D = 3$ mm (circles), $D = 5$ mm (squares) and $D = 10$ mm (diamonds).

where \tilde{X} is the mean value of the elements of \mathcal{D} . The relative error is expressed as a percentage. It is given for the incident wave data in figure 9(a) for the two values of the steepness considered. We find a relative error of approximately 5–7% for all cases, except at $f_0 = 0.7$ Hz, for which it reaches 9%.

We conduct a similar analysis on the vertical displacement of marker 2 to characterize the variability associated with time series obtained from the motion tracking device. For each frequency, wave steepness and disc thickness, we have two measurements corresponding to the two disc locations. Letting A_2 denote the mean value of the fundamental component of the deflection of marker 2 over the steady-state window (obtained by STFT), we define the scaled amplitude $\mathcal{A}_2 = A_2/A$. Under the linearity assumption, this quantity does not depend on the steepness parameter, so that the values obtained for $\varepsilon \approx 1$ and 2% are theoretically the same. Therefore, we conduct our repeatability analysis by calculating the relative error using four values of the scaled displacement \mathcal{A}_2 , corresponding to two disc locations and two steepnesses.

Figure 9(b) shows the relative error of the scaled vertical displacement of marker 2 for the three disc thicknesses considered. We find a relative error of 5% or less in all cases, except for the 5 mm disc (squares), where the error is larger (10–15%) for $f \geq 0.9$ Hz. This suggests that the set-up is more reliable for the 3 and 10 mm discs in this regime. Results for other markers (not shown here) show less variability for the 5 mm disc ($\approx 5\%$ error), so that the variability observed for marker 2 probably arises from local effects. More tests would be required to obtain error estimates with more statistical relevance. However, the results obtained here are satisfactory. In particular, the accuracy of the data is sufficient to conduct relevant comparison analyses with the theoretical predictions.

5. Pointwise comparisons

5.1. Single-disc analysis

We consider the vertical displacement of markers 1, 2, 3 and 4 (see figure 2). The amplitude of each marker is taken to be the mean value of the fundamental component over the steady-state window (STFT method; see §4.1). Scaling each amplitude by the corresponding incident wave amplitude, we define the non-dimensional amplitudes \mathcal{A}_1 , \mathcal{A}_2 , \mathcal{A}_3 and \mathcal{A}_4 , extending the notation introduced in §4.2. These quantities

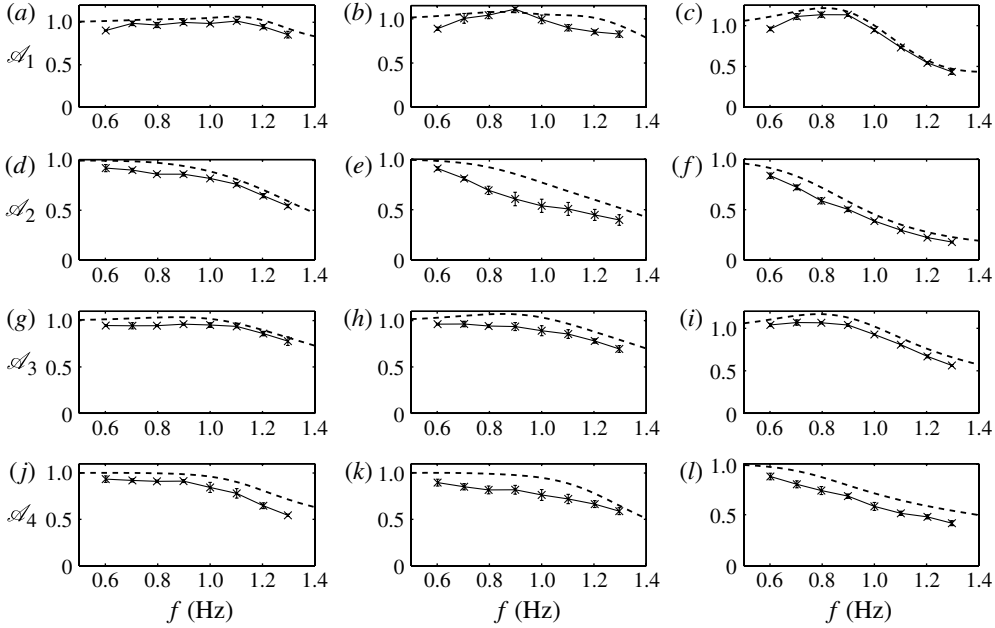


FIGURE 10. Vertical displacement of (a–c) marker 1, (d–f) marker 2, (g–i) marker 3 and (j–l) marker 4 scaled by the incident wave amplitude, as a function of frequency, for the three disc thicknesses considered, i.e. $D = 3$ mm (a,d,g,j), $D = 5$ mm (b,e,h,k) and $D = 10$ mm (c,f,i,l). The experimental data (crosses) include error bars determined using four recorded data for each test. The theoretical data are given continuously as dashed lines over the frequency range $f = 0.5$ – 1.4 Hz.

are estimated theoretically by the modulus of the vertical displacement $|w|$ for an incoming wave of unit amplitude.

Figure 10 shows the scaled vertical displacement of the four markers for each disc thickness considered here. Each experimental data point represents the mean of the scaled amplitudes for four experimental measurements corresponding to two wave steepnesses, $\varepsilon \approx 1$ and 2%, and two disc locations, $x_c \approx 7$ and 10.5 m. Following the repeatability analysis conducted in § 4.2, we include error bars, calculated from the standard deviation of the set of four values. The theoretical data are given in the frequency range $f = 0.5$ – 1.4 Hz. We observe a good general agreement between theory and experiments, particularly for the 3 and 10 mm discs. In most cases, it is seen that the numerical model slightly overestimates the displacement of the disc, however.

The quantitative discrepancy between the experimental data points and the theoretical curve is consistent over the frequency range considered. We find a relative difference $\Delta = 5$ – 20% between theory and experiments for most experimental frequencies. Overall, the agreement is best for the 3 mm disc ($\Delta = 5$ – 10%) and worst for the 5 mm disc ($\Delta = 10$ – 20%). In addition, it is observed that model and experimental data agree best for marker 1 ($\Delta = 5$ – 10%) and worst for marker 4 ($\Delta = 10$ – 20%), which is the only marker not located on the x -axis. This suggests that three-dimensional effects are less accurately represented by the numerical model.

We have obtained local information on the vertical displacement and observed a reasonable agreement although the numerical model consistently overestimates the response. However, we cannot give reliable quantitative estimates regarding the

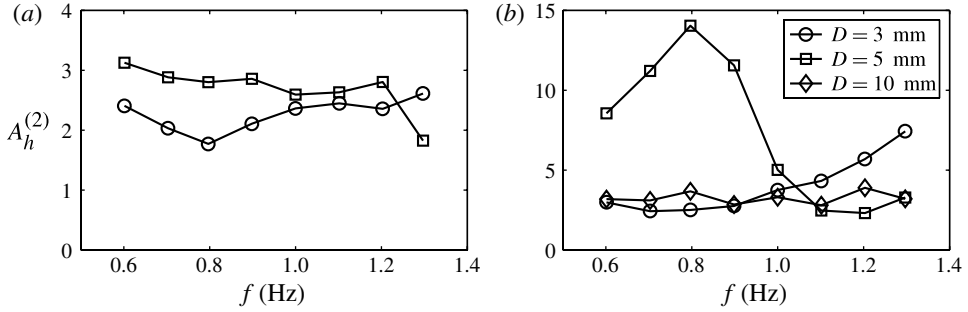


FIGURE 11. Relative second-order relative harmonic for (a) the incident wave amplitude and (b) the vertical displacement of markers 2 (percentage), as a function of frequency. In (a), the data are given for wave steepnesses $\varepsilon \approx 1\%$ (circles) and $\varepsilon \approx 2\%$ (squares). In (b), the data are given for disc thicknesses $D = 3$ mm (circles), $D = 5$ mm (squares) and $D = 10$ mm (diamonds).

flexural motion of the disc using the pointwise analysis. An extension of the present analysis is given in Part 2, in which integrated quantities are considered to measure the bending of the disc.

5.2. Second-order analysis for a single disc

The STFT method, used to process the raw experimental time series (see § 4.1), allows us to analyse the effects of higher-order harmonics on the response. In particular, we may determine how much of the amplitude captured at a measuring point has a nonlinear source. Although we only considered waves of low steepness, nonlinear effects still need to be quantified. A preliminary analysis of the spectrograms associated with the displacement of the disc (not shown here) demonstrated that nonlinearities in the motion are characterized mainly by second-order effects ($f = 2f_0$). Components of higher order are too small to be captured by the measuring devices, and will not be considered in the present analysis.

We determine the proportion of second-order harmonics in the incident wave amplitude and disc displacement. We define the relative second-order harmonic amplitude $A_h^{(2)}$ as the second-order amplitude to fundamental amplitude ratio. This quantity is given in figure 11(a) for the incident wave. We observe that the second-order harmonic, composed of second-order bound and spurious free waves in the basin, represents less than 3% of the fundamental amplitude for most cases considered. The proportion of second-order harmonic is larger for the 2% wave steepness in most cases, as could be expected. It is also seen that for a given steepness, the frequency-dependent data remain reasonably constant over the frequency range considered, which confirms that the wave steepness is the determining parameter for the second-order effects in deep water.

The relative harmonic amplitude of the vertical displacement of marker 2 is plotted in figure 11(b) against frequency for the second-order harmonic only. As in figure 10, each data point represents the mean value over four tests (two steepnesses and two disc locations), theoretically identical when scaled. Error bars are not shown for clarity. In most cases, we find relative harmonic amplitudes similar to those of the incident wave. These second-order effects can be either due to those in the incident wave or generated upon scattering of the incident wave by the disc edge. At low frequencies ($f < 1$ Hz), for $D = 5$ mm, we observe higher relative harmonic

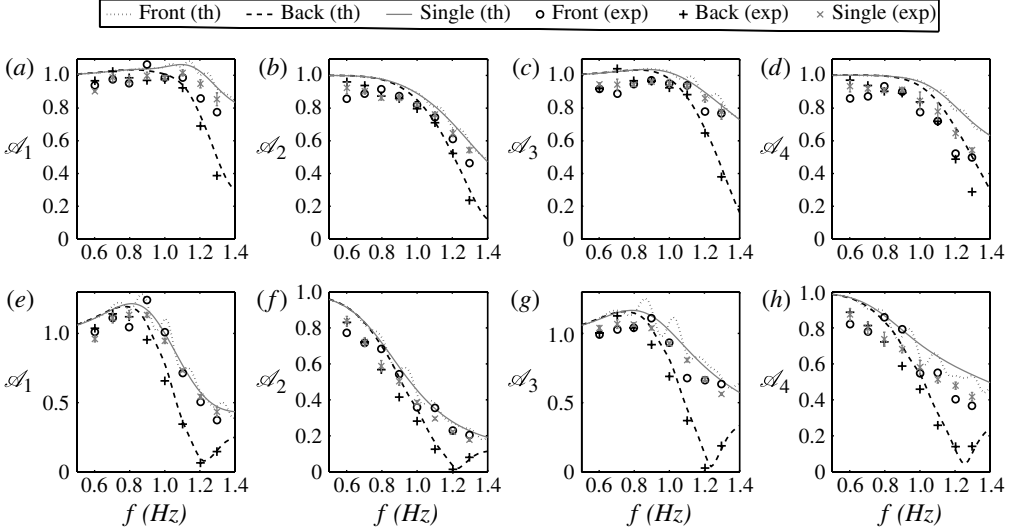


FIGURE 12. Deflection (scaled by the incident wave amplitude) of (a,e) marker 1, (b,f) marker 2, (c,g) marker 3 and (d,h) marker 4 for the two-disc arrangement characterized by the spacing $s = 3$ m and angle $\varpi = 0^\circ$, as a function of frequency. Results are shown for the disc thicknesses (a–d) $D = 3$ mm and (e–h) $D = 10$ mm. Each figure contains the theoretical and experimental data associated with the front disc (dotted lines and circles, respectively), the back disc (dashed lines and pluses, respectively) and the corresponding single disc (solid lines and crosses, respectively).

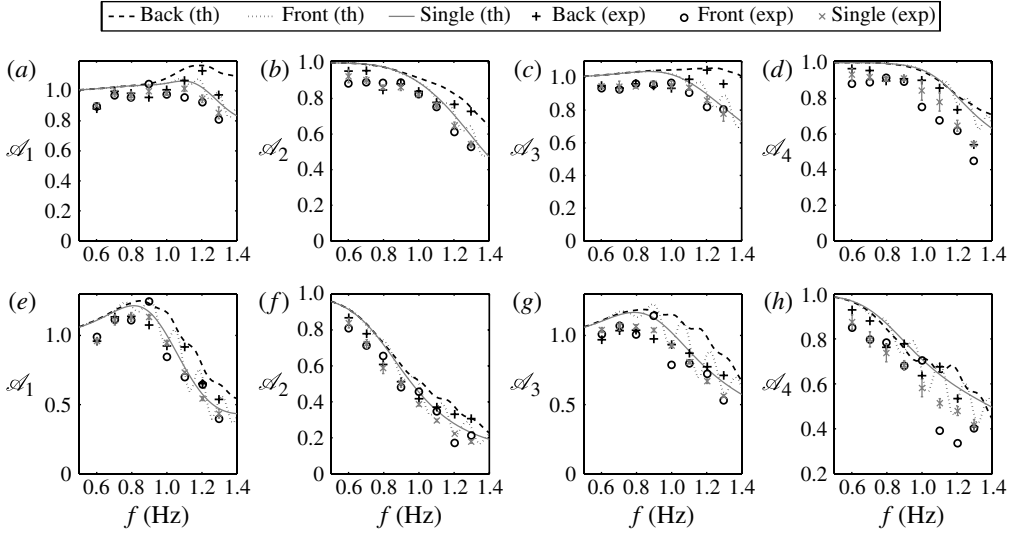
amplitudes (8–15 %), suggesting that additional sources induce second-order motion for this thickness. During the wave basin tests involving the 5 mm disc, we observed visually a resistance to the motion at the disc centre for high-amplitude wave forcing, suggesting the presence of friction. Therefore, we conjecture that the frictional effects along the central rod represent a source of nonlinearities observed in figure 11(b). Note that similar nonlinear effects were observed for other markers.

5.3. Two-disc analysis

Consider the symmetric two-disc arrangement with a 3 m centre-to-centre spacing ($s = 3$ m, $\varpi = 0^\circ$) and the non-symmetric arrangement with a 30° angle ($s = 3$ m, $\varpi = 30^\circ$). We present a model/data comparative analysis for the vertical displacement of markers 1, 2, 3 and 4 of both discs in these two configurations. Note that when the system is rotated from a symmetric arrangement to a non-symmetric arrangement, the four points analysed are rotated by the same angle, so that they are aligned differently with respect to the horizontal axis going through the centres of the discs.

Recall that to define experimental time-harmonic amplitudes, we average the first-order component of the corresponding time series in the steady-state window (see § 4.1), which is chosen to remove the effects of the transient regime and the reflections from the wave basin’s boundaries. For the tests involving two discs, our goal is to determine how the motion in the discs differ from that of a single disc. Therefore, the steady-state window starts after one interaction cycle (i.e. scattered waves travelling from one disc to the other one and back).

Figure 12 shows the theoretical and experimental deflection of the four markers for the symmetric arrangement with spacing $s = 3$ m. Graf’s interaction theory (Kagemoto

FIGURE 13. As figure 12 but for $\varpi = 30^\circ$.

& Yue 1986) is used to incorporate wave interaction between the two discs in the numerical model. The data associated with the front and back discs are compared with those of the single disc for both disc thicknesses considered. At low frequencies ($f < 0.9$ Hz approximately), the two discs do not interact (for both theory and experiments) and both behave as the single disc.

The theoretical data give insights on how the two discs influence each other's response. In particular, we observe that the deflection data of the markers in the front disc oscillate about those of the single disc. We conjecture that the oscillatory behaviour is associated with the natural modes of the hydroelastic system composed of the two plates in a horizontally unbounded fluid domain. It is more difficult to observe these oscillations in the front disc experimental data. The frequency variations are less smooth than those of the single disc, particularly for the 10 mm discs (see figure 12*e–h*), although the variability in the data (not considered here as the tests were not repeated) may explain this behaviour. We obtain a reasonable agreement overall for the front disc, which is quantitatively similar to that discussed in § 5.1 for the single disc.

For $f > 0.9$ Hz, the theoretical data associated with the back disc have significantly lower amplitudes than those of the front disc. This result is sensible as the presence of the front disc alters the incident wave by scattering, so that the back disc undergoes excitations due to waves with reduced energy. For the 10 mm discs (see figure 12*e–h*), we observe a minimum at $f \approx 1.2$ Hz for all four points considered here, suggesting that the back disc is almost immobile. We find a consistent behaviour from the experimental data and, more generally, we obtain a very good agreement between theoretical and experimental data over the frequency range for both thicknesses. These conclusions validate the two-disc experimental set-up in providing reliable data for a symmetric arrangement.

Figure 13 shows the deflection of the four points considered in this analysis for the non-symmetric arrangement with angle $\varpi = 30^\circ$. Similarly to the symmetric arrangement, the low-frequency behaviour shows no signs of interactions between

the discs, and the deflection of theoretical and experimental data in the front disc oscillate about those of the single disc. Note that the theoretical resonances for the front disc markers slightly differ from those of the symmetric case, even though the natural modes of the system are unchanged, as the four points analysed are aligned differently with respect to the axis going through the discs' centres.

At mid to high frequencies, the deflection in the back disc differs significantly from that observed for the symmetric case, as the magnitude of the motion is higher than in the front disc. We will investigate this phenomenon more thoroughly in Part 2. This behaviour is consistent for both theoretical and experimental data, although it is less clear for the experimental data associated with the 10 mm disc (see figure 13e–h). In this case, the deflection data do not vary smoothly over the frequency range. It is unclear whether this behaviour is due to oscillations similar to those in the theoretical data or the variability inherent to the set-up. Nonetheless, the comparisons are satisfactory and allow us to conclude on the validity of the experimental procedure described in § 2.3 for non-symmetric arrangements.

6. Summary and discussions

A unique series of wave basin experiments were conducted at the Laboratoire de recherche en Hydrodynamique, Énergétique et Environnement Atmosphérique of École Centrale de Nantes. The goal of the experimental campaign was to provide benchmark data for the validation of a linear time-harmonic model of wave scattering by one and two circular thin elastic plates with uniform vertical properties. We designed an experimental set-up for compliant discs made of expanded PVC, which adheres to the common restrictions and simplifying assumptions of linear hydroelastic models. Novel technical solutions have been implemented to enforce the restriction of the horizontal motions of the discs and potential flooding events. To measure the deflection of the discs, we deployed an optical remote sensing device that tracks dynamically (using IR cameras) a group of markers fixed on the surface of the disc. For the single-disc set-up, basin tests have been performed for three disc thicknesses, eight wave frequencies, two wave steepnesses and two positions in the basin. For the two-disc set-up, two disc thicknesses, eight frequencies and four arrangements were tested.

After giving a brief description of the numerical model, preliminary comparative results were presented for a single disc using the unprocessed time series provided by the motion tracking device. Reasonable agreement was found for pointwise comparisons of the deflection and visual comparisons of the disc's deflected surface (in phase and amplitude), therefore allowing us to conclude that the experimental set-up provides sensible data.

We then conducted signal processing to ensure the data are consistent with the numerical model's assumptions of linearity, time-harmonicity and unrestricted horizontal domain. A method of time/frequency decomposition was devised to extract the linear component from a raw time series. The method is based on the STFT and allows us to obtain the transient evolution of the filtered linear component of the time series and capture the linear first-order harmonic in a steady-state window, which removes the influence of the transient regime and the basin boundaries.

A repeatability analysis for the incident wave and pointwise deflection measurements showed that the experimental measurements have low variability with less than 8 % relative error in most cases, although the error estimates lack statistical relevance. Additional tests would be required to conclude on the inherent variability of the experimental procedure.

We conducted pointwise model/experiments comparisons of the disc's vertical displacement using processed data. We compared the deflection data at four points of the disc scaled by the incident wave amplitude, over the frequency range considered. We observed a good agreement overall, even though the model consistently overestimates the response for all thicknesses and frequencies, with a relative difference of 5–20 %. The results obtained provide a validation of the STFT method.

Pointwise comparisons were also conducted for a symmetric and a non-symmetric two-disc set-up. Although the discrepancies noted for the single-disc comparisons remained in evidence, we obtained pleasing agreement between model and experiment for the interactions between the discs. In particular, the energy partition between the discs was consistent between theory and experiments.

The discrepancy between theoretical and experimental deflection data for a single disc may originate from different sources. In this paper, we have examined the influence of second-order harmonics on the motion and found that nonlinear effects are low overall. They are less than 5 % of the fundamental amplitude in most cases, and can be explained by nonlinearities inherent to the incident wave and being transferred to the disc motion, or second-order harmonics generated by scattering.

A number of other physical processes may be identified as possible sources of discrepancy between theoretical and experimental data. These arise from processes neglected in the numerical model that are relevant in the experiments or unexpected phenomena occurring due to the disc's experimental equipment. In particular, the influence of the edge barrier on the plate's vibrational behaviour and the frictional effects at the disc's centre due to the central rod need to be analysed further. In addition, we have not determined the validity of the thin elastic plate model to characterize the vibrational behaviour of the discs considered in the experiments. An analysis of these additional processes is proposed in Part 2, where we characterize these effects theoretically to examine how they influence the motion of the disc.

Moreover, although the pointwise comparisons made in this paper are a necessary first step in the analysis, they provide no information on how well the numerical model replicates the flexural motion of the disc. In Part 2, we therefore introduce the natural modes of vibration of the disc *in vacuo*. This will allow us to decompose the displacement of the disc into its rigid-body modes and an infinite set of flexural modes. Further inferences regarding the model/experiment discrepancies will result from this analysis.

Acknowledgements

To complete the work presented in this paper, FM was supported by a University of Otago Doctoral Scholarship. The authors are grateful for the invaluable help provided by technicians of the Laboratoire de recherche en Hydrodynamique, Énergétique et Environnement Atmosphérique of École Centrale de Nantes.

REFERENCES

- ALLEN, J. B. & RABINER, L. R. 1977 A unified approach to short-time Fourier analysis and synthesis. *Proc. IEEE* **65**, 1558–1564.
- ANDRIANOV, A. I. & HERMANS, A. J. 2005 Hydroelasticity of a circular plate on water of finite or infinite depth. *J. Fluids Struct.* **20**, 719–733.
- BISHOP, R. E. D. & PRICE, W. G. 1979 *Hydroelasticity of Ships*. Cambridge University Press.
- CHEN, X., WU, Y., CUI, W. & JENSEN, J. J. 2006 Review of hydroelasticity theories for global response of marine structures. *Ocean Engng* **33**, 439–457.

- CHU, E. 2008 *Discrete and Continuous Fourier Transforms: Analysis, Applications and Fast Algorithms*. Chapman & Hall/CRC.
- COHEN, L. 1989 Time-frequency distributions—a review. *Proc. IEEE* **77**, 941–981.
- FALTINSEN, O. M. & TIMOKHA, A. N. 2009 *Sloshing*. Cambridge University Press.
- HIRDARIS, S. E. & TEMAREL, P. 2009 Hydroelasticity of ships: Recent advances and future trends. *J. Eng. Marit. Environ.* **223**, 305–330.
- KAGEMOTO, H., FUJINO, M. & MURAI, M. 1998 Theoretical and experimental predictions of the hydroelastic response of a very large floating structure in waves. *Appl. Ocean Res.* **20**, 135–144.
- KAGEMOTO, H. & YUE, D. K. P. 1986 Interactions among multiple three-dimensional bodies in water waves: an exact algebraic method. *J. Fluid Mech.* **166**, 189–209.
- KOHOUT, A. L., MEYLAN, M. H., SAKAI, S., HANAI, K., LEMAN, P. & BROSSARD, D. 2007 Linear water wave propagation through multiple floating elastic plates of variable properties. *J. Fluids Struct.* **23**, 643–649.
- LANGHORNE, P. J., SQUIRE, V. A., FOX, C. & HASKELL, T. G. 1998 Break-up of sea ice by ocean waves. *Ann. Glaciol.* **27**, 438–442.
- LOVE, A. E. H. 1944 *A Treatise on the Mathematical Theory of Elasticity*. Dover.
- MARSAULT, P. 2010 Étude des interactions houle/glace de mer. Master's thesis, École Centrale de Nantes (in French).
- MEYLAN, M. H. 1994 The behaviour of sea ice in ocean waves. PhD thesis, University of Otago.
- MEYLAN, M. H. & SQUIRE, V. A. 1996 Response of a circular ice floe to ocean waves. *J. Geophys. Res.* **101**, 8869–8884.
- MONTIEL, F. 2012, Numerical and experimental analysis of water wave scattering by floating elastic plates. PhD thesis, University of Otago.
- MONTIEL, F., BENNETTS, L. G., SQUIRE, V. A., BONNEFOY, F. & FERRANT, P. 2013 Hydroelastic response of floating elastic discs to regular waves. Part 2. Modal analysis. *J. Fluid Mech.* **723**, 629–652.
- OHMATSU, S. 2008 Model experiments for VLFS. In *Very Large Floating Structures* (ed. C. M. Wang, E. Watanabe & T. Utsonomiya). pp. 141–164, Spon Research., chapter 7.
- PETER, M. A., MEYLAN, M. H. & CHUNG, H. 2003 Wave scattering by a circular plate in water of finite depth: a closed form solution. In *Proceedings of the 13th International Offshore and Polar Engineering Conference*, pp. 180–185. The International Society of Offshore and Polar Engineers.
- SAKAI, S. & HANAI, K. 2002 Empirical formula of dispersion relation of waves in sea ice. In *Ice in the Environment: Proceedings of the 16th IAHR International Symposium on Ice*, pp. 327–335. The International Association of Hydraulic Engineering and Research.
- SQUIRE, V. A. 1984 A theoretical, laboratory, and field study of ice-coupled waves. *J. Geophys. Res.* **89**, 8069–8079.
- SQUIRE, V. A. 2007 Of ocean waves and sea-ice revisited. *Cold Reg. Sci. Technol.* **49**, 110–133.
- SQUIRE, V. A. 2008 Synergies between VLFS hydroelasticity and sea ice research. *Intl. J. Offshore Polar Engng* **18**, 241–253.
- SQUIRE, V. A. 2011 Past, present and impendent hydroelastic challenges in the polar and subpolar seas. *Phil. Trans. R. Soc. A* **369**, 2813–2831.
- SUZUKI, H. 2005 Overview of megafloat: Concept, design criteria, analysis, and design. *Mar. Struct.* **18**, 111–132.
- TEN, I., MALENICA, Š & KOROBKIN, A. 2011 Semi-analytical models of hydroelastic sloshing impact in tanks of liquefied natural gas vessels. *Philos. Trans. R. Soc. A* **369**, 2920–2941.
- TOYOTA, T., HAAS, C. & TAMURA, T. 2011 Size distribution and shape properties of relatively small sea-ice floes in the Antarctic marginal ice zone in late winter. *Deep-Sea Res. Pt. II* **58**, 1182–1193.
- UTSUNOMIYA, T., WATANABE, E., WU, C., HAYASHI, N., NAKAI, K. & SEKITA, K. 1995 Wave response analysis of a flexible floating structure by BE-FE combination method. In *Proceedings of Fifth International Offshore and Polar Engineering Conference*, pp. 400–405. The International Society of Offshore and Polar Engineers.

- WANG, C. M., TAY, Z. Y., TAKAGI, K. & UTSUNOMIYA, T. 2010 Literature review of methods for mitigating hydroelastic response of VLFS under wave action. *Appl. Mech. Rev.* **63**, 030802.
- WATANABE, E., UTSUNOMIYA, T. & WANG, C. M. 2004 Hydroelastic analysis of pontoon-type VLFS: a literature survey. *Eng. Struct.* **26**, 245–256.
- WEHAUSEN, J. V. 1971 The motion of floating bodies. *Annu. Rev. Fluid Mech.* **3**, 237–268.
- WU, Y. & CUI, W. 2009 Advances in the three-dimensional hydroelasticity of ships. *J. Eng. Marit. Environ.* **223**, 331–348.
- YAGO, K. & ENDO, H. 1996 On the hydroelastic response of box-shaped floating structure with shallow draft. *J. Soc. Nav. Arch. Japan* **180**, 341–352, (in Japanese).